A new effective way to degrade methylene blue by introducing negative ions powder into Fe_3O_4/H_2O_2 system to accelerate Fe(III)/Fe(II) transformation

Xiangfen Zhang, Hanxin Wu, Zunye Ke, Jiafei Yang, Hongzhou Chen, Feng Xue and Enyong Ding

ABSTRACT

Negative ions powders (NIP) have been widely applied in many fields because of their natural electric field and far infrared radiation, especially in wastewater treatment. In this study, the NIP was first introduced into Fe_3O_4/H_2O_2 system to degrade methylene blue (MB). The MB removal was completely achieved at 5 h *via* a non-photochemical pathway and the degradation rate constant of this system is about 0.565 h^{-1}, which is about 16 times higher than in Fe_3O_4/H_2O_2 Fenton-like system (0.035 h^{-1}). In addition, the results of quenching experiments indicate that the electron (e^-) and negative oxygen ion ($\bullet O_2^-$) are the main reactive species. It was determined that Fe_3O_4@NIP is the effective component that leads to the activation of H_2O_2 to produce •OH, which derive from the pathway: NIP acts as an electron donor to reduce Fe(III) into Fe(II). Moreover, NIP can produce negative ions, which is also conductive to degradation. This study suggests a promising direction for the practical application of NIP based catalysis by integrating it with the Fe(III)/Fe(II) transformation process.

Key words | degradation, dye, isomorphic replacement, negative ions powder

Xiangfen Zhang
Hanxin Wu
Zunye Ke
Jiafei Yang
Hongzhou Chen
Feng Xue
Enyong Ding (corresponding author)
College of Materials Science and Engineering,
South China University of Technology,
Guangzhou 510640,
China
E-mail: *eyding@scut.edu.cn*

HIGHLIGHTS

- The FTIR, XRD, and XPS spectra indicate that the chemical properties of NIP change after the precipitation-hydrothermal process.
- The SEM revealed that Fe_3O_4 was uniformly dispersed in the composite.
- The catalytic activity performance of the Fenton-like system was investigated to remove MB.

INTRODUCTION

To date, dyes are widely used in textile, leather, paper, rubber, plastics, cosmetics, pharmaceutical and food industries and approximately 15% of the world's total production of dyes is lost during the dyeing process and released with the textile effluents (Wang *et al.* 2013a). Hence, from both human and environmental health aspects, the places of the world put more and more emphasis on environmental issues. It is very important to remove dyes from industrial wastewater before they are discharged into the natural environment (Dai *et al.* 2019). Therefore, there is an urgent need to develop a novel environment-friendly catalyst with an excellent activity against organic contaminants in wastewater (Changqiang Yu *et al.* 2020).

Advanced oxidation processes (AOPs) (Cai *et al.* 2014a) based on the generation of highly reactive hydroxyl radicals that present a high redox potential of 2.80 eV (Enric Brillas & Oturan 2009) are generally regarded as a potential

doi: 10.2166/wst.2021.097

alternative technologies for the degradation of recalcitrant contaminants (Cai *et al.* 2014b). In terms of AOPs, the Fenton process is simple, cheap, and easy to perform under moderate conditions of temperature and pressure. But during the Fenton reaction, on the one hand, hydrogen peroxide (H_2O_2) is activated by Fe^{2+} under acidic solution (pH = 3) to produce •OH, so the pH value of the solution can closely affect •OH formation; one the other hand, Fe(II)/H_2O_2 system has some innate shortcomings: active Fe(II) will be rapidly consumed by H_2O_2, which leads to a quick accumulation of inactive Fe(III) because the reaction rate of Fe(II) and H_2O_2 is much higher than that of Fe(III) and H_2O_2 (Equations (1) and (2)) (Wang *et al.* 2013b).

$$Fe^{2+} + H_2O_2 \rightarrow \bullet OH + OH^- + Fe^{3+} \quad k_1 = 70 M^{-1}s^{-1} \tag{1}$$

$$Fe^{3+} + H_2O_2 \rightarrow \bullet OOH + Fe^{2+} + H^+ \quad k_2 = 0.002 - 0.01 M^{-1}s^{-1} \tag{2}$$

To steer clear of this defect, previous researchers have tried to introduce UV or visible radiation to the Fenton system, which would increase the energy in the system and add chelating agents or reducing agents to the Fenton system, which can decrease the Fe(III)/Fe(II) potential and so enhance the product of reactive radicals (Wang *et al.* 2020c). On the removal of diclofenac sodium (DCS) by UV/H_2O_2/Fe^{2+}-based oxidation processes, H_2O_2 generates different radical species under the combined activation of UV and Fe^{2+} when light of sufficient energy is absorbed by an organic molecule (Rehman *et al.* 2020). Chelating agents, such as Ethylenediaminetetraacetic acid and Ethylenediamine-N,N′-disuccinic acid, can also accelerate the transformation of Fe(III) to Fe(II) because the redox potential of Fe(III)/Fe(II) is changed after the addition of chelating agents (Olha *et al.* 2010). As for the reducing agents, hydroxylamine (HA) was proposed to relieve the drawbacks of the Fenton system (Bernd Ensing & Baerends 2003). The g-C_3N_4 was also introduced into the Fe(III)/H_2O_2 system as an electron donor to accelerate Fe(III)/Fe(II) cycling and improve the degradation of organic pollutants under visible light (Xu *et al.* 2020). Besides, due to the special electrochemical properties of Fullerol, from what has been discussed about the Fullerol/Fe(III)/H_2O_2 system (Wang *et al.* 2020c), Fullerol also act as an electron donor to reduce Fe(III) into Fe(II) and accelerate Fe(III)/Fe(II) cycles. These studies show that if a catalyst system can activate Fe(III) or act as electron donor, it may be suitable to add into the Fenton-like system to promote the Fe(III)/Fe(II) transformation.

NIP is a type of inorganic complex material that mainly consists of tourmaline, lanthanide or rare earth elements (Wang *et al.* 2020b) and the strong electronegativity of NIP facilitates the adsorption of the dye. Besides, negative ions can directly purify the air and deodorize. Furthermore, the far-infrared radiation effect of NIP activates water molecules, thereby increasing the oxygen dissolved in the solution, which is advantageous in organic pollutant treatment (Wang *et al.* 2020b). These properties of NIP are closely related to its main ingredient, tourmaline, which is displayed as $XY_3Z_6Si_6O_{18}(BO_3)W_4$, where the X site is commonly taken up by Na^+, K^+, Ca^{2+} or Mg^{2+}; the Y site is occupied by Li^+, Fe^{2+}, Fe^{3+}, Al^{3+}, Mg^{2+} or Ti^{4+}; and the Z site is occupied by Fe^{3+}, Cr^{3+}, Al^{3+}, Mg^{2+} or Fe^{2+}. The W site is often occupied by OH, but it can also be replaced by F or O (Henry & Dutrow 2012). The surface electron generated by isomorphous replacement in the crystal has an important effect on adsorption, but the mechanism needs further study. In tourmaline crystal, there are non-central symmetric unipolar axes, which lead to existence of lone pair electrons and free positive ions in crystallographic structure, and non-coincidence of the positive and negative polar centers in crystal structure lead to permanent electric polarity (Huang *et al.* 2020). Its polar structure enables it to spontaneously adsorb external electric charge as well as charged particles at both poles, and to have intense adsorption to the polar molecule (Zhang 2013). The electric field is formed in a certain range from the tourmaline crystal surface. Under the action of the electric field, neutral molecules are electrolyzed; this increases the content of negative ions (Wang *et al.* 2020a). It is possible that NIP can directly generate electron (e^-) and negative oxygen ion ($\cdot O_2^-$) under dark condition, resulting in the Fe(II) formation. Thereby, NIP may perform well in Fenton-like system to degrade dye.

Herein, we have successfully synthesized the catalyst of Fe_3O_4@NIP composite catalyst by a facile precipitation–hydrothermal process. This work firstly put forward an easy method to improve the catalytic activity of Fe_3O_4 by coupling with the polar mineral NIP, and provide a perfect example for the development of easily synthesized and low-cost NIP-based catalysts. The degradation properties, morphology, pore structure, electron spectrum, magnetism and durability of the samples are characterized and discussed. The abilities of NIP for degrading other dyes have not been extensively studied, and its catalytic activity and mechanisms are not well understood. Therefore, the current research focuses on the catalytic degradation performance of the Fe_3O_4@NIP composite, and a plausible mechanism has been proposed.

MATERIALS AND METHODS

Materials and reagents

Negative ions powder was acquired from Hebei province, China. Ferric chloride ($FeCl_3{\cdot}6H_2O$, analytical reagent) was obtained from Fuchen Chemical Reagent Co, Ltd (Tianjin, China), Ferrous sulfate ($FeSO_4{\cdot}7H_2O$) and sodium hydroxide (NaOH) was obtained from Guangzhou Chemical Reagent Co., Ltd (Guangzhou, China), methylene blue was supplied by Guangzhou Chemical Reagent Co., Ltd (Guangzhou City, China). The Yellow label tea was purchased from Lipton.

Preparation of Fe_3O_4@NIP composite

All reagents were used without further purification or other treatments. Fe_3O_4@NIP composite catalytic materials were prepared by precipitation–hydrothermal method, then were dried (Dai *et al.* 2019) for further use. The preparation of Fe_3O_4 was conducted according to the above method in the case of negative ions powder absence. By using different amounts of Fe_3O_4 (0.5, 1, 2, 3, 4, and 5 mmol, respectively) while keeping the same amount of negative ions powder (4 g), we obtained the composite samples Fx@NIP with different ratios of Fe_3O_4 (x = 0.5, 1, 2, 3, 4, and 5 mmol).

Batch experiment studies

Deionized distilled water was used to prepare all solutions and suspensions. Stock solutions of MB (25 mg/L) were prepared by dissolving measured amounts of the dyes in deionized distilled water. Degradation experiments were conducted using 100 mL of MB solution with a fixed amount of catalyst (0.1 g) and H_2O_2 (30%, v/v). In order to evaluate any real catalytic activity, the adsorption should be excluded. The catalyst-containing solution was maintained in the dark for 0.5 h (Wang *et al.* 2020b) under stirring to achieve adsorption-desorption equilibrium between the pollutant molecules (Yu *et al.* 2019) and the catalyst surface and then added H_2O_2 in the solution. Batch experiments included catalyst type, concentration of H_2O_2, effects of ion species. Further, solution pH variation and the types of reactive species were studied. The purpose was to investigate the catalytic activity and degradation mechanism of dyes by Fe_3O_4@NIP.

Characterization

The catalysts were characterized by FTIR (LEO 1530VP), and their crystallographic nature was analyzed by X-ray diffraction (X'Pert PRO X-ray diffractometer). Their surface morphology was examined by Fifield emission scanning electron microscopy (FE-SEM) with Nova NanoSEM430, while the surface areas were analyzed on the basis of N_2 adsorption-desorption isotherms obtained using a surface area and porosity analyzer (BET, Flowsorb3 2310). The Zeta potential of the catalyst was evaluated using a Zeta potential analyzer. X-ray photoelectron spectroscopy (XPS) was performed on an axis Ultra DLD X-ray Photoelectron Spectroscopy/ESCA. The residual concentrations of the MB were monitored, at its characteristic absorption band (generally 664 nm for MB) using a UV–vis spectrophotometer.

RESULTS AND DISCUSSION

Fourier transform infrared (FTIR) study

It is easy to find the chemical bonds in complex materials by FTIR spectroscopy. As shown in Figure 1, two bands appeared at 3,406 cm^{-1} resulting from the vibration of the −OH groups in NIP (Yu *et al.* 2019). The bending vibration of the Si–O group was detected at 462 cm^{-1}. The band at 400 cm^{-1} – 650 cm^{-1} was due to the M–O (M = Al, Fe, Ti, Si) stretching vibration. A band at 1,027 cm^{-1} stemmed from the C–O stretching vibration (Jastrzębska *et al.* 2016) and Fe–O vibration at 983 cm^{-1} (Liu *et al.* 2016). A well-resolved band at 605 cm^{-1} originated from the Al–O stretching vibration, and was shifted to 612 cm^{-1} with a blue-shift of 7 cm^{-1} for the Fe_3O_4@NIP composite compared with that of the pure NIP. This result implied that NIP could chemically interact with Fe_3O_4 *via* Al–O–Fe bonds. The

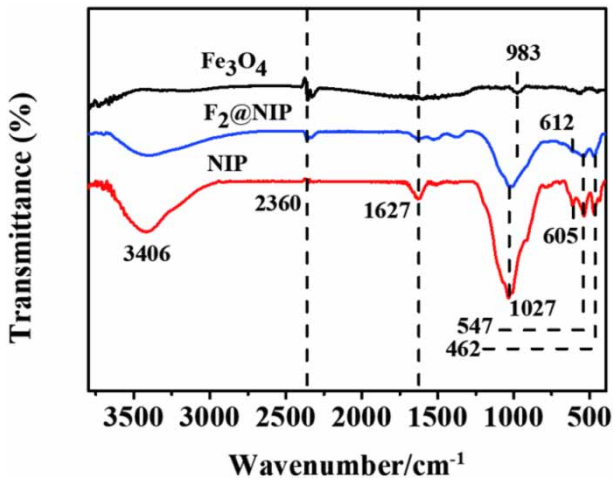

Figure 1 | FTIR spectra of the Fe_3O_4, NIP, and F_2@NIP composite.

presence of water be proved by the absorption peak at 1,627 cm^{-1}, which corresponded to the bending H–O–H (Ghalamchi & Rasoulifard 2019) and the absorption peak at 2,360 cm^{-1} should belong to O = C = O.

CATALYTIC PERFORMANCE

NIP enhanced MB removal in Fe_3O_4/H_2O_2 system

Figure 2(a) shows different degradation rates of MB in various experimental systems at the 3 ml of H_2O_2. It is widely known that a typical organic degradation reaction can be simplified as a pseudo-first order reaction when the initial concentration of reactant is at a low value (Wang *et al.* 2011): $-\ln(C_t/C_0) = kt$, where k is the apparent first-order rate constant (h^{-1}), C_t is the concentration of MB at a certain time (t), and C_0 is the initial concentration of MB. The apparent rate constant (k) can be confirmed by linear regression of the value $\ln(C_t/C_0)$ versus the degradation time (t). The experimental results showed that the activity of F_2@NIP was higher than that of either NIP or Fe_3O_4 as shown in Figure 2(a). It should also be noted that there is only about 1% of MB degradation in the NIP/H_2O_2 system, implying that NIP cannot obviously activate H_2O_2 and generate sufficient active radicals to degrade MB under dark conditions; meanwhile, in Fe_3O_4/H_2O_2 Fenton-like system, there is less than 3% of MB degradation in 5 h. This result in Figure 2(b) depicts that Fe(II) is more active than NIP when reacting with H_2O_2. By contrast, over 99% MB degraded in 5 h in the NIP@Fe_3O_4/H_2O_2 system. As we all know (Xu *et al.* 2020) that the low degradation efficiency is induced by the low conversion of Fe(III) to Fe(II), so the results implied that NIP is favourable to Fe(III)/H_2O_2 oxidation-reduction process. It has also verified that the introduction of Fe_3O_4@NIP can decompose H_2O_2 faster, not only due to the standard Fenton reaction but also due to NIP, which is beneficial to the process of reducing Fe(III) by excluding possible dominant contribution by Fe(III)/Fe(II)-induced H_2O_2 decomposition. As the degradation time increased, the intensity of the absorption peak at approximately 664 nm gradually became weaker and finally disappeared and the results are shown in Figure 2(c), which meant that the chromophore and benzene ring structure of MB were ruined.

Effect of catalyst composition

The degradation of MB was conducted to assess the properties of the different catalyst sample. Figure 2(d) displays the concentration variations of MB (initial concentration: 25 mg/L) under the degradation of catalyst Fx@NIP (x = 0.5, 1, 2, 3, 4, 5 mmol) with 3 ml H_2O_2 which is in line with the pseudo-first order reaction (Figure 2(e)). The results

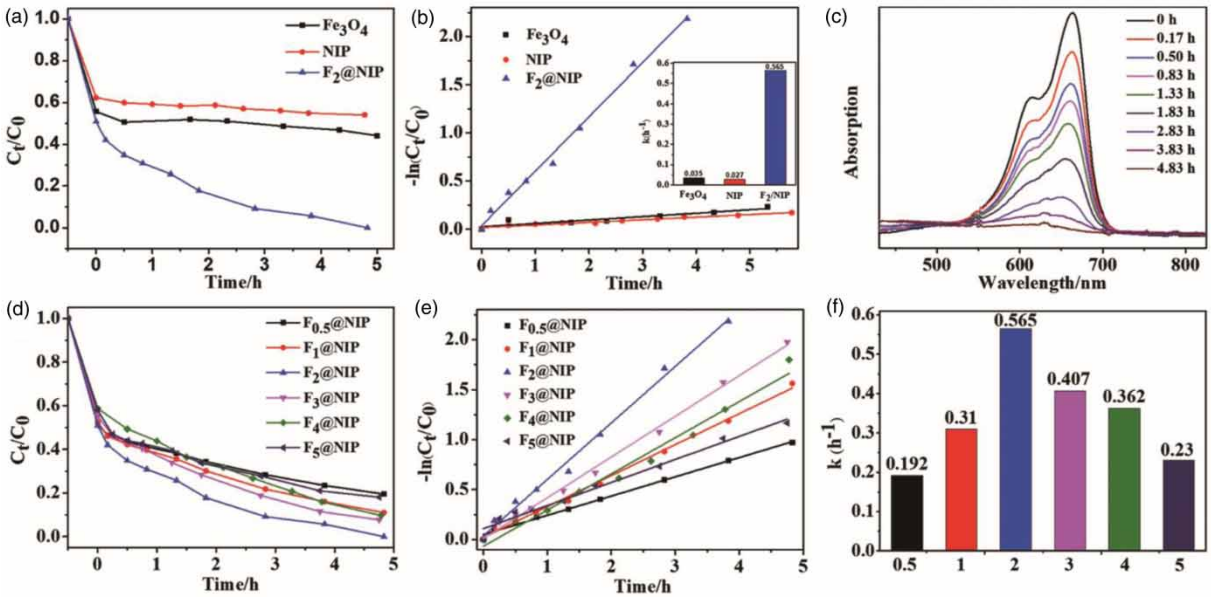

Figure 2 | (a) Degradation of MB by Fe_3O_4, NIP, Fe_3O_4@NIP, (b) The apparent pseudo-first-order kinetic plots, and rate constant k of the Fe_3O_4, NIP, Fe_3O_4@NIP, (c) The absorption of MB at different times, (d) Degradation of MB by Fx@NIP, (e) The apparent pseudo-first-order kinetic plots of the degradation of MB by Fx@NIP, (f) Rate constant k of the Fx@NIP composite degrade MB.

support the fact that the F_2@NIP perform the highest degradation activity (Figure 2(f)). With the increasement dosage of Fe_3O_4, the tendency of degradation efficiency first showed an upward trend and then decreased. This phenomenon can be explained thus: when Fe_3O_4 was less than 2 mmol, the more active points appear on the surface of NIP with the increased molarity of Fe_3O_4; when it is larger than 2 mmol, the number of active points will decrease due to agglomeration, which will lead to smaller special surface area. And the number of active points can directly affect the degradation rate. In comparison with the different catalyst Fx@NIP (x = 0.5, 1, 2, 3, 4, 5 mmol), the F_2@NIP exhibited the highest apparent rate constant (0.565 h^{-1}), which proved that the Fe_3O_4@NIP composite is successfully prepared and show higher catalytic organic oxidation ability with the use of H_2O_2.

Effect of the H_2O_2 concentration

The Fenton system generates free radicals based on decomposition of H_2O_2 catalyzed by Fe(II) (Wang *et al.* 2020c), which indicated that MB degradation depended mainly on the effective decomposition of H_2O_2. As shown in Figure 2(e), H_2O_2 could be decomposed more efficiently even with lower molarity of Fe_3O_4 with the presence of NIP. The higher $[H_2O_2]$ determine faster MB decomposition, which agreed with the faster MB degradation rate in Figure 3(a). However, the rate increment decreased gradually with the increasing dosage of $[H_2O_2]$, as displayed in Figure 3(b). This may be ascribed to the excess H_2O_2 concentration resulting in the reduction of catalytic efficiency by reacting with OH• radicals to produce OOH• radicals (Equation (3)), which is a weaker oxidant agent compared with the much stronger OH• radicals (Mohammadzadeh *et al.* 2020).

$$H_2O_2 + OH\bullet \rightarrow H_2O + OOH\bullet \quad (3)$$

Based on the results, 3 ml of H_2O_2 was used in all experiments.

Effects of inorganic ions on the degradation of MB

Various inorganic ions may co-exist with dye wastewater. Thus, examining the effects of co-existing ions on MB degradation is very important and beneficial for a realistic dye treatment process. Previous researches have confirmed that the presence of some inorganic ions in the catalytic system could affect the adsorption or degradation of dye (Zhou *et al.* 2019). Cations can interact with negatively charged mineral surfaces by purely electrostatic attraction. Such reactions are

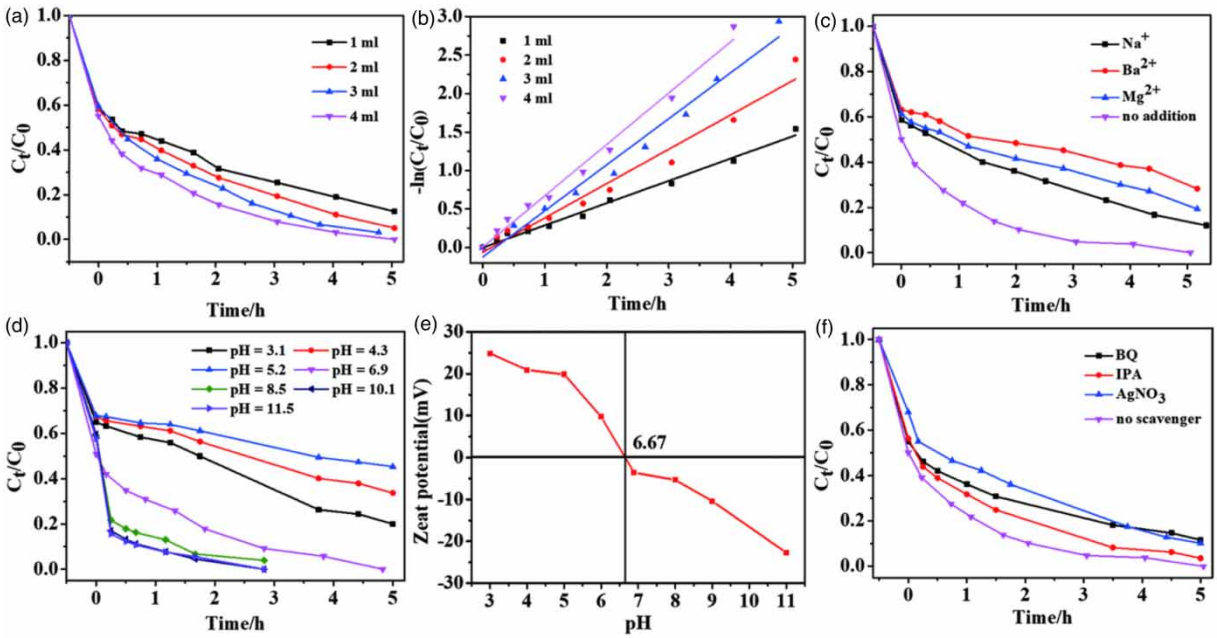

Figure 3 | (a) (b) Influence on MB degradation and the apparent pseudo-first-order kinetic plots with different H_2O_2 dosage, (c) effects of inorganic cations on MB degradation. Experimental conditions: no pH adjustment (original pH = 6.86); $[Na^+] = 40$ mM, $[Ba^{2+}] = 40$ mM, and $[Mg^{2+}] = 40$ mM. (d) (e) MB degradation and Zeta potential of the F_2@NIP composite with different initial solution pH. (f) MB degradation over the F_2@NIP composite with different reactive species scavengers. Experimental conditions: [IPA] = 10 mM, [BQ] = 0.2 mM, $[AgNO_3] = 50$ μM.

well-known for cation interactions with permanently charged mineral surfaces. The usually weak electrostatic nature of cation attachment to permanently charged surfaces renders this interaction readily reversible and strong competition with other cations takes place (Geckeis *et al.* 2013). Considering that natural water does not contain buffer solution, and that the introduction of buffer solution will make the degradation system more complicated, the influence of inorganic ions was not investigated in buffer solution (Luo *et al.* 2020). The influence of inorganic cations on the degradation of MB in the NIP@Fe_3O_4/H_2O_2 heterogenous Fenton- like system was investigated at the cation concentration of 40 Mm. As shown in Figure 3(c), inorganic cations, including Na^+, Ba^{2+} and Mg^{2+}, exhibited an inhibitory effect on the degradation of MB, and it was determined that the adsorption affinities of different alkaline earth ions at the Fe_3O_4@NIP surfaces decline in the order of $Ba^{2+} > Mg^{2+} > Na^+$. The greater the adsorption of inorganic cations, the less of MB, which leads to a decrease in the degradation rate. We all know how important it is to consider not only the effect of the ions interacting with the mineral surface, but also the bulk solvent phase (Underwood *et al.* 2016). So the ionic dipole interaction and hydration need to consider when the cations were added into solution. The ionic dipole interaction of different metal ions in bulk solutions depends on the ionic radius. So the studied inorganic ions are known to decline in the order of $Ba^{2+} > Na^+ > Mg^{2+}$, and the greater the dipole interaction between ions and mineral surface, the greater the adsorption. Meanwhile the hydration effects of different metal ions in bulk solutions are known to decline in the order of $Na^+ > Mg^{2+} > Ba^{2+}$ and the greater the hydration, the less ions are adsorbed on the mineral surface. Hydration will play a major role in a low electric field and ionic dipole interaction will take the lead in a high electric field (Jia *et al.* 2018). Hence, the preliminary results indicated that the surface of NIP has a low electric field. The varied absorption of cations depends on different hydration, which leads to poor adsorption and weak degradation of MB. At the same time, the accompanying shielding effect, with reduction in the number of active sites, also caused the low catalytic efficiency (Qian *et al.* 2018).

Degradation efficiency of F_2@NIP at different pH values

The solution pH plays an important part in heterogeneous Fenton-like systems because it can influence the electrostatic interactions between reactant molecules and the catalyst surface, metal leaching and H_2O_2 decomposition (Hanna *et al.* 2008). When Zeta potential of the mineral surface is 0, the pH value of the solution is called the isoelectric point (pH_{iep}). The isoelectric point is the dividing point to confirm whether a mineral surface is negatively or positively charged. When the solution's $pH > pH_{iep}$, it shows the mineral surface is negatively charged; in the reverse, it is positively charged. Different pH of solution resulted in different degradation effects of MB and surface potential of catalyst (Figure 3(d) and 3(e)). The isoelectric point of the F_2@NIP composite was determined to be $pH = 6.67$. When the pH value of the solution was less than 6.67, the adsorption between the positively charged composite and the positively charged MB was weakened by electrostatic repulsion, and the acidic condition may decelerate the ionization of H_2O and H_2O_2, so fewer OH^- exist near the active sites of the catalyst, which causes reduction of hydroxyl radicals derived from OH^- oxidation (Bian & Ji 2015). However, at the same time, as the pH of the solution decreased, a few [Fe^{2+}] that can be released from Fe_3O_4 showed a faster catalytic reactivity. Generally, the degradation rate of MB decreased under acidic conditions. Judging from the experiment, it showed that pH values of the solution larger than 6.67 were more conducive to degradation. The reason for this result was probably that the adsorption between the negatively charged composite and the positively charged MB is strengthened by electrostatic attraction in an alkaline environment; moreover, the possibility of isomorphic replacement is greater, which will produce more negative charge on the surface of the NIP. For example (Equation (4)), NIP crystals have Al^{3+} replaced by Fe^{2+}, which will create one negative charge.

$$NIP(Al^{3+}) + Fe^{2+} \rightarrow NIP(Fe^{2+})_{(surface)}e^- + Al^{3+} \quad (4)$$

Negative zeta potential increases with pH (Figure 3(e)). This was not only because the material has stronger adsorption to the outside, which promotes the electrolysis of a higher number of H_2O_2 and H_2O, thus increasing the number of negative ions (Wang *et al.* 2020a), but also because the more isomorphous replacements occurs, the more electrons are produced, thus increasing the number of free radicals. F_2@NIP Fenton-like catalyst has an advantage of working over a wider pH range compared with the traditional one, which is limited to $pH < 4$ (Bernd Ensing & Baerends 2003). Under natural conditions, the pH of the MB solution was 6.89 and according to the zeta potential of the Fx@NIP composites at various pH values, it was easy to judge that the surface of F_2@NIP is negatively charged, so F_2@NIP composites can efficiently adsorb MB, which can improve degradation rate.

Study of active species

The types of reactive species produced in the Fe_3O_4@NIP/H_2O_2 system were determined using isopropanol (IPA) as hydroxyl radical (•OH) scavenger, benzoquinone (BQ) as a superoxide radicals ($•O_2^-$) scavenger, and $AgNO_3$ as electron (e^-) scavenger (Kaveh *et al.* 2020). It was found that IPA had little effect on MB removal in this system. However, $AgNO_3$ and BQ showed a significant inhibitory effect on MB degradation as shown in Figure 3(f). These results indicated that e^- and $•O_2^-$ was the predominant reactive species in the process of the MB degradation, while a mild reduction in MB degradation was observed by hindering hydroxyl radical reactive species. In this work, the degradation system was maintained under constant air-equilibrated conditions, indicating that the abundant O_2 from air promoted the formation of $•O_2^-$, resulting in its high catalytic efficiency (Chen & Liu 2017). The results also confirmed that NIP could promote the reduction of Fe(III) as an electron donor, thus accelerating H_2O_2 decomposition and MB degradation. The mechanisms will be discussed later (Equation (10)).

Morphological and structural characterizations of catalyst

Figure 4(a) and 4(b) demonstrate SEM images of the F_2@NIP particles with different parts, and the agglomeration of the sample is observed. Moreover, with the EDS spectrum in Figure 4(c), the purpose was to further explore the dispersion of Fe_3O_4 in NIP. A certain area was intercepted arbitrarily in the SEM image, there was an apparent oxygen element peak in the elemental composition map, and the area was about 6 μm^2. Representative elements of Fe_3O_4 and NIP were presented in such a small range and it indicated to some extent that Fe_3O_4 can be relatively uniformly dispersed in NIP under this preparation process (Luo *et al.* 2019). The EDS spectrum also showed the presence of C, O, P, Fe, Al, Si, Ti and Th elements in the sample. The Cu and Au signals were owing to the SEM grid used for the imaging.

The XRD patterns of Fe_3O_4, NIP and Fx@NIP (x = 0.5, 1, 2, 3, 4, 5 mmol) are shown in Figure 5. The diffraction peaks at $2\theta = 30.1$, 35.4, 43.2, 54.0, 56.8 and 62.5

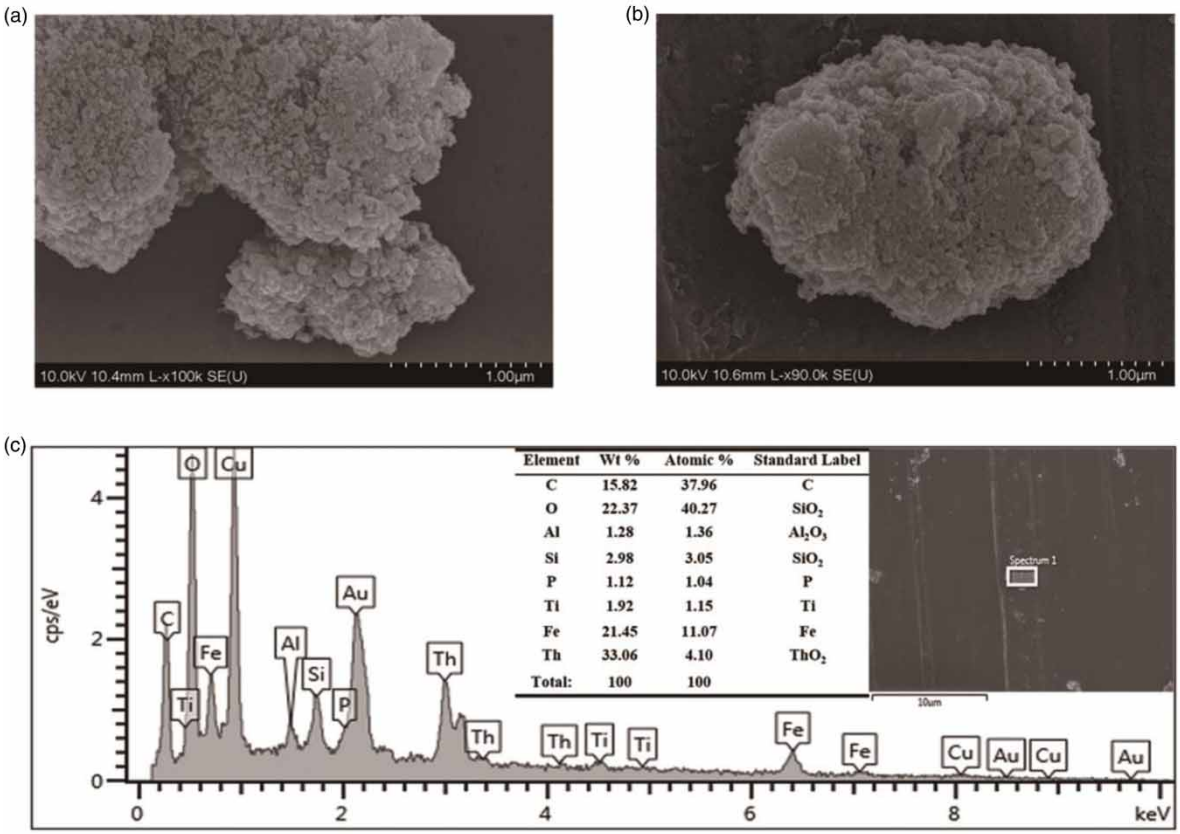

Figure 4 | (a) (b) The SEM images, (c) EDS analysis of F_2@NIP.

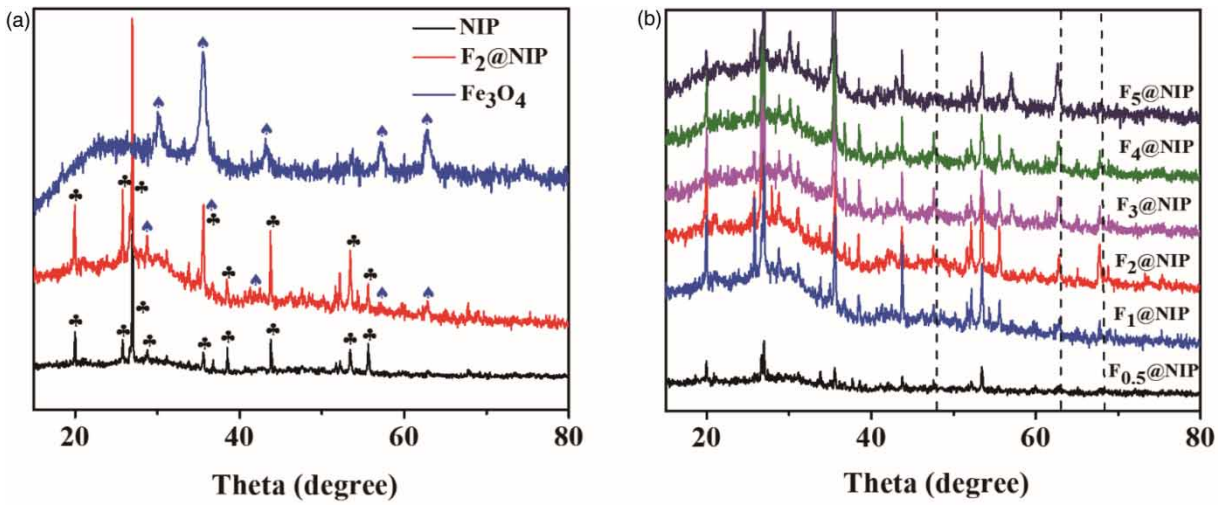

Figure 5 | XRD patterns of the as-prepared samples, (a) NIP, Fe_3O_4 and (b) Fx@NIP (x = 0.5, 1, 2, 3, 4, 5).

correspond to the (220), (311), (400), (422), (511), and (440) planes of Fe_3O_4 (Tan *et al.* 2019) (JCPDS No.19-0629), respectively. As for NIP, the diffraction peaks were sharp and intensive, indicating a highly crystalline phase in the sample. The XRD patterns of Fx@NIP could be perfectly indexed as the inverse spinal structure of magnetite Fe_3O_4. And the peaks in the XRD patterns of the Fx@NIP coincided almost completely with those of the Fe_3O_4 and NIP raw materials (Figure 5(a)), which indicted that Fx@NIP has been successfully synthesized. We also noticed that with increasing mass of Fe_3O_4, the diffraction peak intensity for Fe_3O_4 at $2\theta = 62.5$ enhanced (Figure 5(b)), the diffraction peak narrowed and the grain size increased. This demonstrated that the lesser mass of Fe_3O_4 of the composite materials result in grain refinement; in turn, this resulted in a larger specific surface area that maximized the effect of the raw materials. The XRD patterns revealed that the diffraction peaks of the composite materials had shifted slightly to the left; moreover, the d-spacing increased or decreased to varying degrees compared with the original materials (Wang *et al.* 2020a). This indicated that Fe_3O_4 caused slight crystal defects or crystal doping of raw materials.

BET, XPS and VSM analysis

The BET surface areas of NIP, F_2@NIP composites and pure Fe_3O_4 are given in Figure 6(a). The BET surface area of the F_2@NIP sample was much higher than that of NIP and the pure Fe_3O_4. According to the IUPAC classification, the isotherm of F_2@NIP composite material showed that it is a typical mesoporous material with H3 hysteresis loop type IV isotherm (Inagaki *et al.* 1995). This indicated that the catalyst is composed of aggregates of cubic particles, forming pores of uneven size and shape (Bakre *et al.* 2016). This conclusion is in agreement with the SEM image. The F_2@NIP composites showed larger average pore size and pore volume than NIP (Table 1). The pore size distribution (Figure 6(b)) implied that F_2@NIP presented a relatively narrow distribution with an average pore diameter close to 2.049 nm. The experimental results showed that Fe_3O_4-doped NIP possesses a larger BET specific surface area and pore volume compared with pure NIP. Moreover, it was confirmed that F_2@NIP composite owns an incremental number of active sites.

Based on the data in Figure 2(a), the active constituent in the Fe_3O_4/H_2O_2 system increased greatly after the addition of NIP. There may be some interaction between NIP and Fe_3O_4, which increases the production of Fe(II) in the system, resulting in acceleration of active constituent generation. The surface element component and valence state of the as-synthesized catalysts were investigated with XPS. The Fe $2p_{3/2}$ presents two peaks: Fe^{2+} at 709.3 eV and Fe^{3+} at 711.2 eV, and Fe $2p_{1/2}$ also presents two peaks: Fe^{2+} at 718.5 eV and Fe^{3+} at 723.3 eV in pure Fe_3O_4 (Crişan *et al.* 2018). From the deconvolution result of the Fe peaks in the spectrum (Figure 6(c)), in comparison with pure Fe_3O_4, the binding energy of Fe $2p_{3/2}$ and Fe $2p_{1/2}$ for the Fe_3O_4@NIP composite was shifted to 711.60 eV and 724.55 eV, respectively. The evidence of the chemical interaction between Fe_3O_4 and NIP accords with the results of XRD analysis.

Figure 6(d) demonstrates the hysteresis loop of F_2@NIP and F_5@NIP at room temperature. The saturation

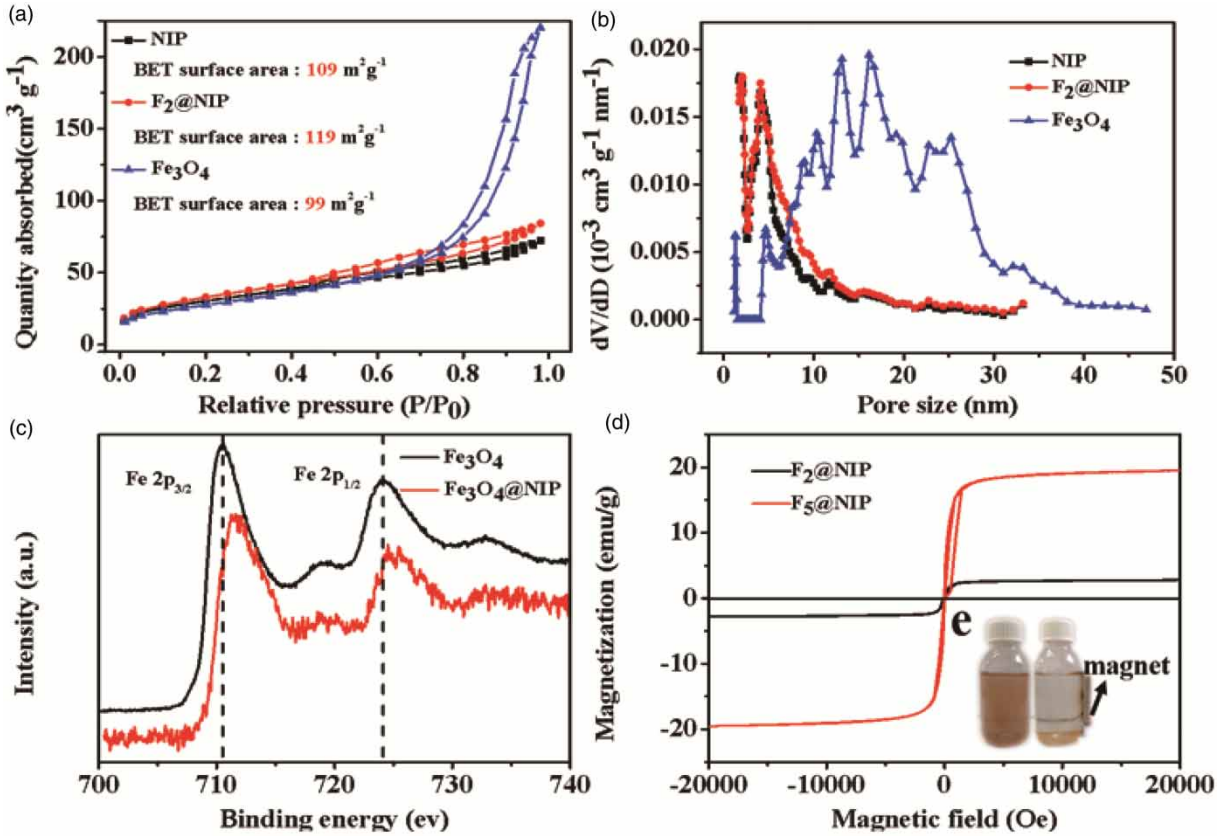

Figure 6 | (a) (b) N_2 adsorption/desorption isotherm and pore size distribution of the NIP, the F_2@NIP composites and Fe_3O_4, (c) high-resolution Fe 2p XPS spectra of the Fe_3O_4 and F_2@NIP composite, (d) magnetization curves of F_2@NIP and F_5@NIP at room temperature, (e) the suspension of F_2@NIP solution before and after applied with an external magnet.

Table 1 | The pore parameters of the NIP, the F_2@NIP composites and pure Fe_3O_4

Sample	Total pore area ($cm^3\ g^{-1}$)	Average pore size (nm)
NIP	0.104	1.848
F_2@NIP	0.122	2.049
Fe_3O_4	0.324	16.142

magnetizations were 2.67 emu/g and 19.51 emu/g for F_2@NIP and F_5@NIP, respectively. Obviously, a much stronger Hall effect could be obtained in F_5@NIP than in F_2@NIP (Tan *et al.* 2019), resulting in the different catalytic performances as have been discussed above. For the good magnetic property, the F_2@NIP could be easily separated from the mixture using a magnet, as shown in the Figure 6(e).

The reusability of Fe_3O_4@NIP

Stability of the catalyst in the successive applications is critical for practical usage. The reusability of Fe_3O_4@NIP was also researched, and the results are presented in Figure 7. It can be seen that catalysts slowly deactivated with time. After four repetitions, the degradation efficiency was still high, as shown in Figure 7(a), implying that Fe_3O_4@NIP had good stability and reusability. As shown in Figure 7(b), the well-resolved band at 612 cm^{-1} originated from the Al–O stretching vibration, which was shifted to 622 cm^{-1} with a blue-shift of 10 cm^{-1}, and the band at 1,027 cm^{-1} originated from the C–O stretching vibration, which was shifted to 1,039 cm^{-1} with a blue-shift of 12 cm^{-1} for the F_2@NIP composite that had degraded four times compared with that of the untouched F_2@NIP. The infrared absorption intensity of the used catalyst was slightly lower than that of the untouched catalyst. The shift of peak position and the change of peak absorption intensity in the fingerprint region provided evidence for isomorphism replacement. It was also found that the amount of MB desorbed from catalyst decreased gradually after each process of degradation and ethanol washing. That might be related to the loss of surface area; in addition, as the number of catalyst reuses increased, isomorphous replacement of NIP is likely to become less and variable charge decreases. That all could

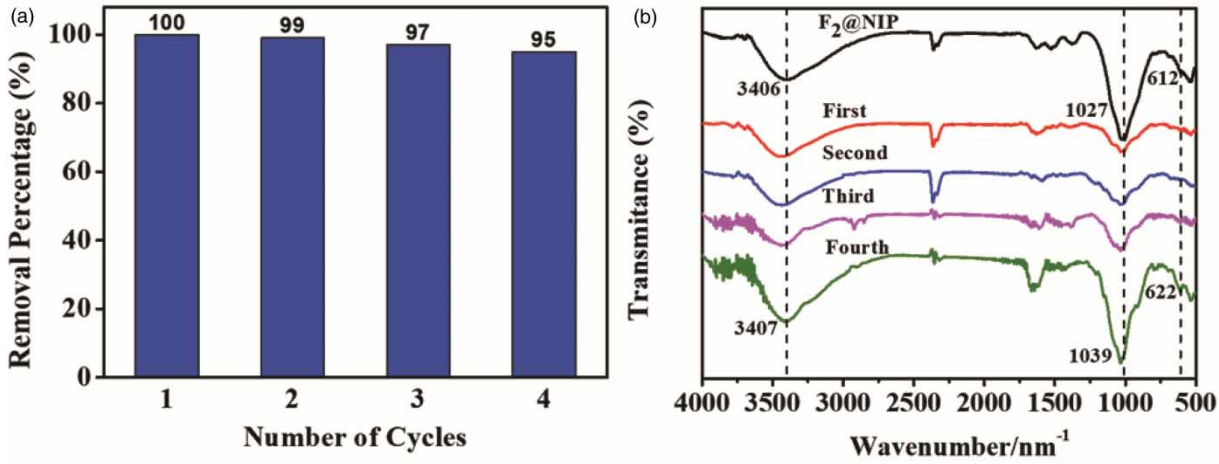

Figure 7 | (a) Four successive catalytic MB degradation (%) cycles over the F_2@NIP composite. (b) IR patterns of F_2@NIP composite: four successive catalytic MB degradations and unused F_2@NIP.

lead to a gradual deterioration in the catalytic performance of the catalyst. But the efficiency of degradation was still higher than the Fe_3O_4/TiO_2 system (Ghalamchi & Rasoulifard 2019) and Fe-tourmaline system (Wang *et al.* 2013a). The NIP contains a certain amount of thorium dioxide and it appears likely, though not entirely verified, that the stable catalysts may be attributed to thorium, the solids that kept the surface area during the reaction (João Lúis Rangel Costa & Rangel 2002). After each repetition of the test, the F_2@NIP sample was washed with deionized water and ethanol 3 times, and heated at 80°C for 3 h.

EFFECT MECHANISM OF NIP ON THE CATALYTIC ACTIVITY OF FE_3O_4/H_2O_2

Far infrared radiation of NIP

Far infrared rays serve the purpose, by being absorbed in water clusters. If the radiation wavelength of far infrared rays accords with the absorption wavelength of an object to be irradiated, molecules in the object absorb the radiations at that wavelength, causing stretching and deformation due to the resonance, and the molecules are brought to a place where it becomes easier to react (Feng & Shang 2015). We have studied the effects of Fe_3O_4@NIP on the infrared emissivity. Tea leaves of the same mass were added to the Fe_3O_4@NIP treated deionized water and ordinary deionized water, and the tea leaves soaking conditions were observed at different times (Figure S1, ESI†). From the experimental results, it can be seen that the color of treated water is darker (Figure S1a,c, ESI†), indicating that the activity of treated water molecules is higher than that of ordinary deionized water, so this will be favorable for tea soaking. An implication of this is the possibility that Fe_3O_4@NIP will reduce the van der Waals forces and destroy the hydrogen bonding force between the water molecules, which may lead the clusters of liquid water to change from large to small (Equations (5) and (6)) compared with ordinary deionized water.

Natural electric field of NIP

Fine NIP just has a natural peculiarity that can offer a spontaneous and permanent polarity to produce an electrostatic field and can generate negative oxygen ion($\bullet O_2^-$) (Equation (9)), which is a big advantage in enhancing the catalytic activity of catalysts containing NIP. For one thing, the resulting electrostatic interaction between NIP and molecules or ions plays an important role in the process of degradation; for another, the electric field of the NIP can impel charges to move in a certain range when the surface of the Fe_3O_4@NIP releases charges from isomorphous replacement (the ion being replaced could be Al^{3+}, shown as Equation (4)). Based on an increase in the electron density compared with pure Fe_3O_4, the electric field generated on the surface of NIP led directional transportation of the generated electron (e^-) (Yu *et al.* 2019), thus enhancing the catalytic activity. Due to the ability to release electrons (e^-) (Equation (10)), NIP could rapidly reduce Fe(III) in the presence of H_2O_2. The fast transformation of Fe(III)/Fe(II) is the key factor to induce the generation of •OH (Equation (12)). The spontaneous electric field would promote the electron

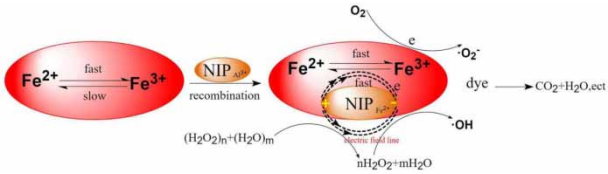

Figure 8 | Schematic illustration of the role of NIP in enhancing the catalytic activity of Fe_3O_4/H_2O_2.

transfer process and minimize the resistance of the transfer from Fe(III) to Fe(II), although further research is required regarding the mechanism responsible (Yu *et al.* 2014). The half-life of thorium is 7,340 years. During the process of radioactive decay, the α-particles collide with the atoms and molecules in the solution. This may be beneficial to the effects of the degradation though it has not been entirely verified (Alam *et al.* 2020). Therefore, NIP can increase the catalytic activity of the Fe_3O_4/H_2O_2 system.

$$\mathrm{NIP} + (H_2O)_m \rightarrow \mathrm{NIP} + m\ H_2O \quad (5)$$

$$\mathrm{NIP} + (H_2O_2)_n \rightarrow \mathrm{NIP} + n\ H_2O_2 \quad (6)$$

$$\mathrm{NIP_{(surface)}}e^- + H_2O \rightarrow \mathrm{NIP} + \bullet OH + H^+ \quad (7)$$

$$\mathrm{NIP_{(surface)}}e^- + H_2O_2 \rightarrow \mathrm{NIP} + \bullet OOH + H^+ \quad (8)$$

$$\mathrm{NIP_{(surface)}}e^- + O_2 \rightarrow \mathrm{NIP} + \bullet O_2^- \quad (9)$$

$$\mathrm{NIP_{(surface)}}e^- + Fe^{3+} + H_2O_2 \rightarrow \mathrm{NIP} + Fe^{2+} + \bullet OH + H^+ \quad (10)$$

$$Fe^{3+} + \bullet OOH \rightarrow Fe^{2+} + H^+ + O_2 \quad (11)$$

$$Fe^{2+} + H_2O_2 \rightarrow Fe^{3+} + OH^- + \bullet OH \quad (12)$$

Hence, the addition of NIP can speed up the transformation of Fe(III)/Fe(II) by non-photochemical pathways and activate H_2O_2, which will all generate •OH and $\bullet O_2^-$ to remove MB. With a combination of the analyses carried out above, a plausible mechanism for strengthening the catalytic degradation activity of Fe_3O_4/H_2O_2 with NIP is proposed and shown in Figure 8.

CONCLUSIONS

Taken together, these findings indicated that under dark conditions, the addition of NIP to the Fe_3O_4/H_2O_2 system could greatly promote the degradation of MB. This study is the first comprehensive investigation of how the NIP works in the system. In this work, we found that the surface of NIP has a low electric field that could mildly activate H_2O and H_2O_2; moreover, electrons (e^-) can be generated by isomorphous replacement in the system of Fe_3O_4@NIP/H_2O_2. The released electrons not only favor the production of $\bullet O_2^-$ but also the production of Fe(II). A large amount of Fe(II) formed in the system contributed to the production of •OH and boosted the degradation of the system. The application of Fe_3O_4@NIP composites in engineering has not been studied. In the future, the pyroelectric effect and piezoelectric effect of Fe_3O_4@NIP composites will be further explored to broaden their application.

DATA AVAILABILITY STATEMENT

All relevant data are included in the paper or its Supplementary Information.

REFERENCES

Alam, I., Rehman, J. U., Ahmad, N., Nazir, A., Hameed, A. & Hussain, A. 2020 An overview on the concentration of radioactive elements and physiochemical analysis of soil and water in Iraq. *Rev. Environ. Health* **35** (2), 147–155.

Bakre, P. V., Volvoikar, P. S., Vernekar, A. A. & Tilve, S. G. 2016 Influence of acid chain length on the properties of TiO_2 prepared by sol-gel method and LC-MS studies of methylene blue photodegradation. *J. Colloid Interface Sci.* **474**, 58–67.

Bernd Ensing, F. B. & Baerends, E. J. 2003 Fenton-like chemistry in water: oxidation catalysis by Fe(III) and H_2O_2. *J. Phys. Chem. A* **107**, 5722–5731.

Bian, X. & Ji, R. 2015 Photocatalytic degradation of methyl blue by tourmaline-coated TiO_2 nanoparticles. *Desalin. Water Treat.* **57** (41), 19292–19300.

Cai, C., Wang, L., Gao, H., Hou, L. & Zhang, H. 2014a Ultrasound enhanced heterogeneous activation of peroxydisulfate by bimetallic Fe-Co/GAC catalyst for the degradation of Acid Orange 7 in water. *J. Environ. Sci.* **26** (6), 1267–1273.

Cai, C., Zhang, H., Zhong, X. & Hou, L. 2014b Electrochemical enhanced heterogeneous activation of peroxydisulfate by Fe-Co/SBA-15 catalyst for the degradation of Orange II in water. *Water Res.* **66**, 473–485.

Changqiang Yu, M. W., Tong, Z., Li, S., Yin, Y., Liu, X., Li, Y., Liang, T., Wu, Z. & Dionysiou, D. D. 2020 Synthesis and enhanced photocatalytic performance of 0D/2D CuO/tourmaline composite photocatalysts. *Beilstein J. Nanotechnol.* **11**, 407–416.

Chen, Y. & Liu, K. 2017 Fabrication of magnetically recyclable Ce/N co-doped $TiO_2/NiFe_2O_4$/diatomite ternary hybrid: improved photocatalytic efficiency under visible light irradiation. *J. Alloys Compd.* **697**, 161–173.

Crişan, M., Mardare, D., Ianculescu, A., Drăgan, N., Niţoi, I., Crişan, D., Voicescu, M., Todan, L., Oancea, P., Adomniţei, C., Dobromir, M., Gabrovska, M. & Vasile, B. 2018 Iron doped TiO_2 films and their photoactivity in nitrobenzene removal from water. *Appl. Surf. Sci.* **455**, 201–215.

Dai, H., Huang, Y., Zhang, Y., Zhang, H. & Huang, H. 2019 Green and facile fabrication of pineapple peel cellulose/magnetic diatomite hydrogels in ionic liquid for methylene blue adsorption. *Cellulose* **26** (6), 3825–3844.

Enric Brillas, I. S. s. & Oturan, M. A. 2009 Electro-Fenton process and related electrochemical technologies based on Fenton's reaction chemistry. *Chem. Rev.* **109**, 6570–6631.

Feng, Y. W. & Shang, Y. P. 2015 Effects of fine tourmaline particles on photocatalytic activity of nano-sized TiO_2 powders. *Mater. Res. Innovations* **19** (sup10), S10–160–S10–3.

Geckeis, H., Lutzenkirchen, J., Polly, R., Rabung, T. & Schmidt, M. 2013 Mineral-water interface reactions of actinides. *Chem. Rev.* **113** (2), 1016–1062.

Ghalamchi, L. & Rasoulifard, M. H. 2019 Immobilization of Fe_3O_4/TiO_2 nanocomposite thin layer on the glass tubes in a component parabolic collector for the treatment of DR23. *International J. Environ. Sci. Technol.* **16** (11), 7509–7522.

Hanna, K., Kone, T. & Medjahdi, G. 2008 Synthesis of the mixed oxides of iron and quartz and their catalytic activities for the Fenton-like oxidation. *Catal. Commun.* **9** (5), 955–959.

Henry, D. J. & Dutrow, B. L. 2012 Tourmaline at diagenetic to low-grade metamorphic conditions: its petrologic applicability. *Lithos* **154**, 16–32.

Huang, S.-M., Weng, C.-H., Tzeng, J.-H., Huang, Y.-Z., Anotai, J., Yen, L.-T., Chang, C.-J. & Lin, Y.-T. 2020 Photocatalytic inactivation of *Klebsiella pneumoniae* by visible-light-responsive N/C-doped and N-tourmaline/palladium-C-codoped TiO_2. *Chem. Eng. J.* **379**.

Inagaki, S., Fukushima, Y. & Miyata, M. 1995 Inclusion polymerization of isoprene in the channels of sepiolite. *Res. Chem. Intermed.* **21** (2), 167–180.

Jastrzębska, A. M., Karcz, J., Letmanowski, R., Zabost, D., Ciecierska, E., Zdunek, J., Karwowska, E., Siekierski, M., Olszyna, A. & Kunicki, A. 2016 Synthesis of the r-GO/Al_2O_3 core–shell nanocomposite flakes and characterization of their unique electrostatic properties using zeta potential measurements. *Appl. Surf. Sci.* **362**, 577–594.

Jia, Z., Li, X., Zhu, C., Yang, S. & Yang, G. 2018 Reversal of cation-specific effects at the interface of mica and aqueous solutions. *J. Phys. Chem. C* **122** (10), 5358–5365.

João Lúis Rangel Costa, G. S. M. & Rangel, M. d. C. 2002 A thorium-doped catalyst for the high temperature shift reaction. *Catal. Today* **77**, 205–213.

Kaveh, R., Mokhtarifar, M., Bagherzadeh, M., Lucotti, A., Diamanti, M. V. & Pedeferri, M. 2020 Magnetically recoverable TiO_2/SiO_2/gamma-Fe_2O_3/r-GO composite with significantly enhanced UV-visible light photocatalytic activity. *Molecules* **25** (13).

Liu, J., Meng, J., Liang, J., Zhang, H. & Gu, X. 2016 Effect of tourmaline-doped on the far infrared emission of iron ore tailings ceramics. *J. Nanosci. Nanotechnol.* **16** (4), 3777–3780.

Luo, Y., Chen, Q., Wang, C. & Guo, T. 2019 Preparation and improved negative ion release of graphene/tourmaline composite. *Mater. Res. Express* **6** (5).

Luo, W., Huang, W., Feng, X., Huang, Y., Song, X., Lin, H., Wang, S. & Mailhot, G. 2020 The utilization of Fe-doped g-C_3N_4 in a heterogeneous photo-Fenton-like catalytic system: the effect of different parameters and a system mechanism investigation. *RSC Adv.* **10** (37), 21876–21886.

Mohammadzadeh, A., Khoshghadam-Pireyousefan, M., Shokrianfard-Ravasjan, B., Azadbeh, M., Rashedi, H., Dibazar, M. & Mostafaei, A. 2020 Synergetic photocatalytic effect of high purity ZnO pod shaped nanostructures with H_2O_2 on methylene blue dye degradation. *J. Alloys Compd.* **845**.

Olha, S., Furman, A. L. T. & Watts, R. J. 2010 Mechanism of base activation of persulfate. *Environ. Sci. Technol.* **44**, 6423–6428.

Qian, X., Wu, Y., Kan, M., Fang, M., Yue, D., Zeng, J. & Zhao, Y. 2018 FeOOH quantum dots coupled g-C_3N_4 for visible light driving photo-Fenton degradation of organic pollutants. *Appl. Catal. B Environ.* **237**, 513–520.

Rehman, F., Ahmad, W. & Sayed, M. 2020 Mechanistic investigations on the removal of diclofenac sodium by UV/$S_2O_8^{2-}/Fe^{2+}$, UV/HSO_5^-/Fe^{2+} and UV/H_2O_2/Fe^{2+}-based advanced oxidation processes. *Environ. Technol* 1–11.

Tan, J., Wang, X., Hou, W., Zhang, X., Liu, L., Ye, J. & Wang, D. 2019 Fabrication of Fe_3O_4@graphene/TiO_2 nanohybrid with enhanced photocatalytic activity for isopropanol degradation. *J. Alloys Compd.* **792**, 918–927.

Underwood, T., Erastova, V. & Greenwell, H. C. 2016 Ion adsorption at clay-mineral surfaces: the Hofmeister series for hydrated smectite minerals. *Clays Clay Min.* **64** (4), 472–487.

Wang, D., Baral, J. K., Zhao, H., Gonfa, B. A., Truong, V.-V., El Khakani, M. A., Izquierdo, R. & Ma, D. 2011 Controlled fabrication of PbS quantum-dot/carbon-nanotube nanoarchitecture and its significant contribution to near-infrared photon-to-current conversion. *Adv. Funct. Mater.* **21** (21), 4010–4018.

Wang, C., Zhang, Y., Yu, L., Zhang, Z. & Sun, H. 2013a Oxidative degradation of azo dyes using tourmaline. *J. Hazard. Mater.* **260**, 851–859.

Wang, Q., Tian, S. & Ning, P. 2013b Degradation mechanism of methylene blue in a heterogeneous Fenton-like reaction catalyzed by ferrocene. *Ind. Eng. Chem. Res.* **53** (2), 643–649.

Wang, C., Chen, Q., Guo, T. & Li, Q. 2020a Environmental effects and enhancement mechanism of graphene/tourmaline composites. *J. Cleaner Prod.* **262**.

Wang, X., Jian, J., Yuan, Z., Zeng, J., Zhang, L., Wang, T. & Zhou, H. 2020b In situ loading of polyurethane/negative ion powder composite film with visible-light-responsive Ag_3PO_4@AgBr particles for photocatalytic and antibacterial applications. *Eur. Polym. J.* **125**.

Wang, Y., Zhou, P., Wang, Q., Huo, X., Huang, X., Ye, Q., Xu, H., Zhou, G., Liu, Y. & Zhang, J. 2020c Fullerol mediated enhancement of chloramphenicol degradation in Fe(III)/H_2O_2 system by accelerating Fe(III)/Fe(II) cycle via a non-photochemical pathway. *Chem. Eng. J.* **402**.

Xu, H., Ye, Q., Wang, Q., Zhou, P., Huo, X., Wang, Y., Huang, X., Zhou, G. & Zhang, J. 2020 Enhancement of organic contaminants degradation at low dosages of Fe(III) and H_2O_2 in g-C_3N_4 promoted Fe(III)/H_2O_2 system under visible light irradiation. *Sep. Purif. Technol.* **251**.

Yu, L., Wang, C., Ren, X. & Sun, H. 2014 Catalytic oxidative degradation of bisphenol A using an ultrasonic-assisted tourmaline-based system: influence factors and mechanism study. *Chem. Eng. J.* **252**, 346–354.

Yu, C., Tong, Z., Li, S. & Yin, Y. 2019 Enhancing the photocatalytic activity of ZnO by using tourmaline. *Mater Lett.* **240**, 161–164.

Zhang, J. 2013 The role of tourmaline particles in the moving bed bioreator for coking wastewater treatment. *Appl. Mech. Mater* **321–324**, 192–195.

Zhou, G., Wang, Y., Zhou, R., Wang, C., Jin, Y., Qiu, J., Hua, C. & Cao, Y. 2019 Synthesis of amino-functionalized bentonite/$CoFe_2O_4$@MnO_2 magnetic recoverable nanoparticles for aqueous Cd^{2+} removal. *Sci. Total Environ.* **682**, 505–513.

First received 16 December 2020; accepted in revised form 4 March 2021. Available online 16 March 2021